ADVANCING EARTH AND SPACE SCIENCES

JGR Solid Earth

RESEARCH ARTICLE
10.1029/2026JB033955

# Time Dependence of Multiple Geomagnetic Surface Intensity Minima

**Yaochen Yue**[1,2,3], **Filipe Terra-Nova**[4], **Hagay Amit**[3], **Victor Marum**[3,5], **Yuqi Wang**[1,2], and **Yong Wei**[1,2]

[1]Key Laboratory of Earth and Planetary Physics, Institute of Geology and Geophysics, Chinese Academy of Sciences, Beijing, China, [2]College of Earth and Planetary Sciences, University of Chinese Academy of Sciences, Beijing, China, [3]Laboratoire de Planétologie et Géosciences, Nantes Université, University Angers, Le Mans Université, CNRS, Nantes, France, [4]Université Paris Cité, Institut de Physique du Globe de Paris, CNRS, Paris, France, [5]Instituto de Geociências, Universidade Estadual de Campinas, Campinas, Brazil

**Key Points:**

- We introduce a topological algorithm to identify geomagnetic surface intensity extrema and saddle points
- The algorithm allows for the first time calculation of sub-region areas of surface intensity anomalies
- Modern SAA split is charaterized by shrinkage of the primary minimum and expansion of the secondary minimum

**Supporting Information:**

Supporting Information may be found in the online version of this article.

**Correspondence to:**

Y. Wei,
weiy@mail.iggcas.ac.cn

**Citation:**

Yue, Y., Terra-Nova, F., Amit, H., Marum, V., Wang, Y., & Wei, Y. (2026). Time dependence of multiple geomagnetic surface intensity minima. *Journal of Geophysical Research: Solid Earth*, *131*, e2026JB033955. https://doi.org/10.1029/2026JB033955

Received 3 FEB 2026
Accepted 17 JUL 2026

**Author Contributions:**

**Conceptualization:** Yaochen Yue, Filipe Terra-Nova, Hagay Amit, Yong Wei
**Data curation:** Yaochen Yue, Filipe Terra-Nova
**Formal analysis:** Yaochen Yue, Hagay Amit
**Funding acquisition:** Yong Wei
**Investigation:** Yaochen Yue, Filipe Terra-Nova, Hagay Amit
**Methodology:** Yaochen Yue, Filipe Terra-Nova, Hagay Amit
**Project administration:** Yong Wei
**Software:** Yaochen Yue, Filipe Terra-Nova
**Supervision:** Filipe Terra-Nova, Hagay Amit, Yong Wei
**Validation:** Yaochen Yue
**Visualization:** Yaochen Yue, Hagay Amit
**Writing – original draft:** Yaochen Yue, Filipe Terra-Nova, Hagay Amit, Victor Marum, Yuqi Wang, Yong Wei



**Abstract** The present-day geomagnetic field is characterized by a region of weak intensity over the South Atlantic, known as the South Atlantic Anomaly (SAA). Since 2008, the SAA has split with a new local minimum appearing in Africa. This split introduces a challenge for characterizing the time dependence of multiple minima, particularly their respective areas. In this work, we propose a new topological algorithm to calculate the time-dependent areas and centers of complex field configurations with multiple local surface intensity minima enclosed by the same threshold value. The algorithm relies on the identification of saddle points, which enables for the first time the subdivision of the SAA area into sub-regions associated with different minima. In addition, we analyze contours of null intensity gradient, which do not require setting an arbitrary threshold value. Based on the modern geomagnetic field model, we find that the sub-region area associated with the weaker South America minimum decreases, whereas that of the Africa minimum increases. Both minima drift westward, though the primary South America minimum drifts four times faster. The historical field reveals the emergence of an earlier Pacific anomaly, while the archeomagnetic field indicates recurrent expansion of the total anomaly region and anti-correlation of sub-region area evolutions over the past millennium. Finally, the null meridional intensity gradient tends to the Southern Atlantic, while the azimuthal gradient exhibits an order-2 signature suggestive of mantle control on the geomagnetic field.

**Plain Language Summary** The South Atlantic Anomaly (SAA) is a region where Earth's magnetic field is unusually weak, which can affect satellites and space technology. In recent years, the SAA has split into two separate weak-field minima, one over South America and a newer over Africa. Although this split has been widely observed, it has been difficult to interpret because previous studies mainly described the SAA as a single region and lacked tools to examine its morphology. In this study, we introduce a new topological approach that separates the SAA into sub-regions associated with each weak-field minimum, allowing to track changes in their areas and positions over time. We show that the area linked to the primary South America minimum has been shrinking, while that associated with the newer Africa minimum has been expanding. Furthermore, by analyzing null intensity gradient components we find stronger non-dipole field in the Southern Atlantic responsible for the locations of surface minima. Our results suggest that surface magnetic anomalies reflect large-scale processes deep within the Earth.

## 1. Introduction

The geomagnetic field shields our planet from solar wind and cosmic rays (Arsenović et al., 2024; Pan & Li, 2023). However, in regions of weak intensity, the flux of high-energy particles and radiation is increased (Gao et al., 2022; Heirtzler, 2002; Olson & Amit, 2006), posing significant risks to spacecrafts. Exposure to such radiation when passing through the weak intensity regions can damage onboard electronic systems and cause malfunctioning of spacecraft components (Meier et al., 2023). These unique space environments might also give rise to unusual space weather phenomena, such as low-latitude aurora (He et al., 2020, 2021; Wang et al., 2021). In addition, the geomagnetic field contributes to maintaining a habitable environment on Earth (Erdmann et al., 2021; Olson & Amit, 2006), for example, by preventing the erosion of the atmosphere (Rao, 1980; Wei et al., 2014). Studies of weak intensity anomalies provide insights into Earth's interior processes by relating small-scale details of the geodynamo to the surface field (Campuzano et al., 2019; Hulot et al., 2002; Tarduno

10.1029/2026JB033955

**Writing – review & editing:** Yaochen Yue, Filipe Terra-Nova, Hagay Amit, Victor Marum, Yuqi Wang, Yong Wei

et al., 2015; Terra-Nova & Amit, 2025; Terra-Nova et al., 2017, 2019; Trindade et al., 2018). Therefore, a detailed characterization of these surface anomalies and their temporal variation is essential, both for a fundamental understanding of core dynamics as well as for societal applications such as the design and long-term operation of spacecraft instrumentation.

Earth's magnetic field varies over a wide range of timescales (e.g., Finlay et al., 2010). At certain times, the geomagnetic field exhibits regions of anomalously weak intensity at Earth's surface. The most prominent anomaly in the historical era is the South Atlantic Anomaly (SAA) (Bloxham et al., 1989; Campuzano et al., 2019; De Santis & Qamili, 2015; Finlay et al., 2025; Nilsson et al., 2022; Olson & Amit, 2006; Schanner et al., 2023; Terra-Nova & Amit, 2025), where the field intensity reaches a minimum of about 22 μT. The SAA is evolving rapidly, characterized by weakening, expansion, and westward drift (Amit et al., 2021; Finlay et al., 2020; Terra-Nova et al., 2017). However, its temporal variation is more complex, including short episodes of nearly steady areas and eastward drift (Amit et al., 2021; Hartmann & Pacca, 2009).

The time dependence of surface intensity anomalies is commonly described by tracking their center and area. To define the anomaly area, fixed intensity threshold values are often set, for example, 30 μT or 32 μT for the SAA (Amit et al., 2021; Finlay et al., 2020) or 36 μT for the paleo-West Pacific Anomaly (WPA) (He et al., 2021; Yue et al., 2024). The choice of a threshold value affects the inferred rate of change of the SAA area (Finlay et al., 2025). Furthermore, the field intensity outside the SAA region should be accounted to adjust the anomaly region boundary according to the overall strength of the global magnetic field (Amit et al., 2021). When the global field becomes weaker, a lower threshold value is required to define the anomaly region boundary, whereas a stronger field corresponds to a higher threshold. This normalization ensures that the boundary evolves consistently with the long-term variation of the global field. As a result, the inferred areal expansion becomes somewhat slower (Amit et al., 2021) than that obtained using a fixed intensity threshold (Finlay et al., 2025).

The position of the SAA center has traditionally been described using the global minimum of the geomagnetic field intensity (e.g., Hartmann & Pacca, 2009; Pavón-Carrasco & De Santis, 2016; Terra-Nova et al., 2017). In order to assess the geographical recurrence of surface minima, Terra-Nova et al. (2019) averaged the distribution of local minima centers by accounting for their intensity over millennial timescales based on archeomagnetic field models. They identified preferred longitudes, including one in agreement with the present-day SAA longitude. However, persistent latitudes were often significantly lower than the latitude of the present-day SAA. Yue et al. (2024) applied the local minima to characterize another weak intensity anomaly, the WPA, which reached a minimum of about 34 μT, exhibited complex drift patterns associated with emergence, splitting and disappearance episodes in the historical era. The WPA splitting process is similar to that inferred for the SAA. Moreover, the WPA has been shown to be recurrent over millennial timescales (Tema et al., 2023). These approaches simply identified locations of either global or local minima by searching for grid points in which intensity is lower than that of surrounding neighbors. In contrast, Amit et al. (2021) calculated the center of mass (CM) which captures the effect of non-isotropic distribution (see also Amit et al., 2010).

Based on numerical dynamo simulations that approach Earth's outer core dynamical state, Aubert (2015) predicted that the SAA will continue expanding and weakening. However, since around 2008, the SAA has exhibited a new feature: a secondary minimum rapidly weakening near southern Africa (Finlay et al., 2020, 2025; Rother et al., 2021; Sanchez et al., 2020; Terra-Nova et al., 2019). One study has attempted to predict the time dependence of these two local minima in the South Atlantic. Sanchez et al. (2020) suggested that the eastern secondary minimum may further develop and potentially become the dominant minimum within the next few decades. A similar split event was reported for the WPA (Yue et al., 2024). The detailed morphological field changes leading to the splitting of surface intensity minima have yet to be demonstrated.

In this work, we propose a new topological algorithm to identify and calculate centers and areas of surface intensity minima. Intersections of the null intensity gradient contours are employed to locate all extrema and saddle points. This approach enables for the first time the subdivision of the SAA into two sub-regions, each associated with a separate local minimum. It can also be applied to other surface intensity anomalies, such as the WPA. Furthermore, the distribution of null intensity gradient contours provides new insights into non-dipole features and hemispheric asymmetry in the geomagnetic field.

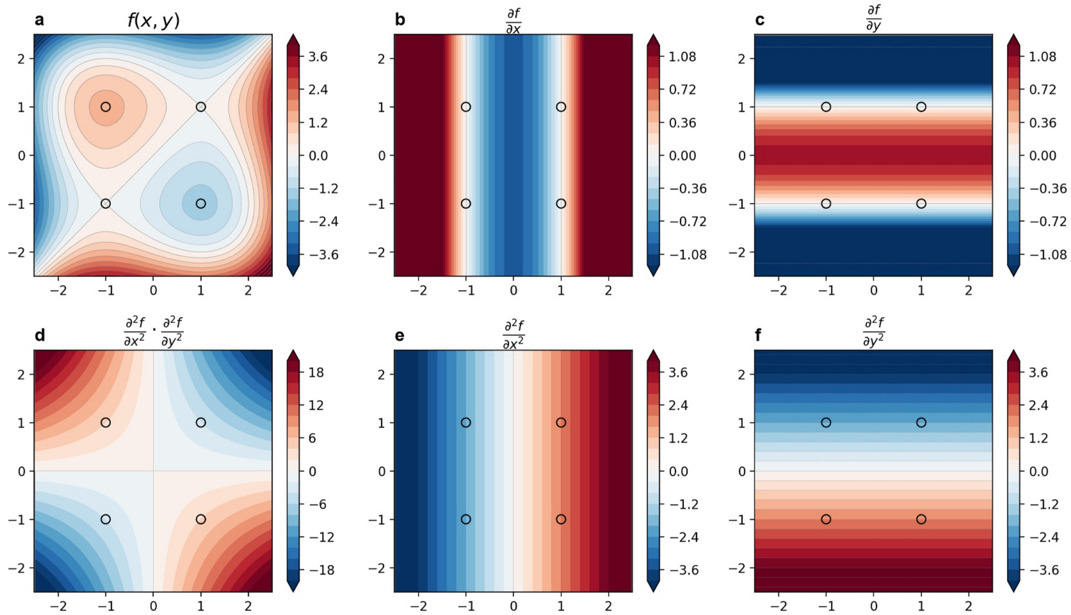


**Figure 1.** The synthetic 2D function (a), its first-order spatial derivatives (b and c), second-order spatial derivatives (e and f) and their product (d). Circles denote extrema and saddle points.

## 2. Methods

In this section, we describe two main calculations: characterization of surface intensity minima (Sections 2.1 and 2.2) and analysis of null gradient contours (Section 2.3). We present a new topological algorithm developed to properly characterize the centers and areas of multiple geomagnetic surface intensity minima at a given time. This algorithm provides a framework for investigating the time-dependence of regions containing multiple surface intensity minima, such as the present-day SAA (Terra-Nova et al., 2019).

First, we describe the detection of local extrema and saddle points within these regions (Section 2.1). Next, we describe the determination of the total anomaly region and sub-regions where the intensity is considered weak (Section 2.2). The saddle points are then used to define the areas of sub-regions associated with pairs of surface intensity minima enclosed by the same threshold contour, as well as their corresponding centers of mass. Finally, we describe the analysis of topologies of intensity gradient null contours (Section 2.3).

### 2.1. Extrema and Saddle Points Identification

The appearance of a secondary minimum in the SAA around 2008–2010, (depending on the studied model and the choice of spatial truncation) has drawn the attention of numerous studies (Finlay et al., 2020; Rother et al., 2021; Sanchez et al., 2020; Terra-Nova et al., 2019). Such field topology might be challenging for the characterization of the surface intensity minima. Most notably, it is not clear how to partition the total area that encompasses two minima in order to attribute an area to each minimum. In this section, we propose a formalism to calculate the areas of the two minima based on the location of the saddle point between them. To systematically identify all critical points, including extrema (minima, maxima) and saddle points between extrema, we propose a topological method applicable to any two-dimensional scalar field.

For clarity, we begin by illustrating the method with a synthetic example. Consider the following 2D function in Cartesian coordinates:

$$f(x,y) = \left(\frac{x^3}{3} - x\right) - \left(\frac{y^3}{3} - y\right) \tag{1}$$

As shown in Figure 1a, this function displays two extrema (one minimum and one maximum) and two saddle points. These critical points are characterized by zero first derivatives: $\frac{\partial f}{\partial x}$ (Figure 1b) and $\frac{\partial f}{\partial y}$ (Figure 1c). Saddle points are located in regions where $\frac{\partial^2 f}{\partial x^2} \cdot \frac{\partial^2 f}{\partial y^2} < 0$, whereas both extrema lie in regions where this product is positive (Figure 1d). This mathematical criterion provides a simple and effective means to identify and distinguish between different types of critical points. In spherical coordinates the extrema and saddle points identification is:

$$\begin{cases} \frac{\partial F}{\partial \theta} = 0 \\ \frac{\partial F}{\partial \phi} = 0 \\ \frac{\partial^2 F}{\partial \theta^2} \cdot \frac{\partial^2 F}{\partial \phi^2} < 0 \end{cases} \Rightarrow \text{saddle point} \tag{2}$$

$$\begin{cases} \frac{\partial F}{\partial \theta} = 0 \\ \frac{\partial F}{\partial \phi} = 0 \\ \frac{\partial^2 F}{\partial \theta^2} \cdot \frac{\partial^2 F}{\partial \phi^2} > 0 \end{cases} \Rightarrow \text{extrema point} \tag{3}$$

The contours of $\frac{\partial F}{\partial \theta} = 0$ and $\frac{\partial F}{\partial \phi} = 0$ are extracted using the *Matplotlib python library* (Hunter, 2007). Each contour is represented as a series of discrete off-grid points with a spatial resolution of $1^\circ \times 1^\circ$. To determine the location where $\frac{\partial F}{\partial \theta} = 0$ and $\frac{\partial F}{\partial \phi} = 0$ contours cross, linear fits are applied between adjacent points along each contour, expressed as $\theta = a_{\frac{\partial F}{\partial \theta}}\phi + b_{\frac{\partial F}{\partial \theta}}$ and $\theta = a_{\frac{\partial F}{\partial \phi}}\phi + b_{\frac{\partial F}{\partial \phi}}$. Two segments that overlap in both longitude and latitude are identified. Then linear fits are performed for the two segments along the $\frac{\partial F}{\partial \theta} = 0$ and $\frac{\partial F}{\partial \phi} = 0$ contours to determine their intersection.

Intersection points with co-latitudes outside the range between 5° to 175° are excluded to avoid possible numerical problems associated with the polar regions. Although the precise locations of intersection points are off the original grid points, their accuracy depends on the resolution of the input field model.

### 2.2. Areas and Centers

A fixed intensity threshold value is commonly employed to define the boundary of weak-field regions. A value of 32 μT for the modern SAA (De Santis et al., 2013; Pavón-Carrasco & De Santis, 2016) was motivated by space safety considerations, whereas 36 μT allows to monitor the less intense WPA (He et al., 2021). However, to focus on regional field time dependence, variations in the intensity of the global field over time should also be taken into account. Following Amit et al. (2021) and Yue et al. (2024), the parameter $F_{out}$ is adopted to represent the normalized magnetic intensity outside the anomalies weak-field region. This parameter reflects the background field strength. Amit et al. (2021) calculated $F_{out}$ based on the intensity in the entire northern hemisphere and the Pacific southern hemisphere, a choice that is adequate for the modern SAA. However, over longer periods surface intensity anomalies may reside elsewhere, for example the west Pacific (He et al., 2021; Tema et al., 2023; Yue et al., 2024). Considering that weak anomalies typically occur at low latitudes (Terra-Nova et al., 2019), we therefore define $F_{out}$ as the high-latitude areas, specifically between 65° and 90°(shown as black shadings at high latitudes in Figure 2a):

$$F_{out}(t) = \frac{\int_{0^\circ}^{360^\circ}\int_{0^\circ}^{25^\circ} F(t) \sin\theta \, d\theta \, d\phi + \int_{0^\circ}^{360^\circ}\int_{155^\circ}^{180^\circ} F(t) \sin\theta \, d\theta \, d\phi}{\int_{0^\circ}^{360^\circ}\int_{0^\circ}^{25^\circ} F(t_0) \sin\theta \, d\theta \, d\phi + \int_{0^\circ}^{360^\circ}\int_{155^\circ}^{180^\circ} F(t_0) \sin\theta \, d\theta \, d\phi} \tag{4}$$

where $F(t_0)$ denotes the value of $F$ in the reference year $t_0$. We selected the highest 25° latitudes to avoid overlap with the present-day SAA area. The anomaly region is defined as the area where the intensity falls below a critical value $F_c$, given by

$$F_c(t) = F_0 \cdot F_{out}(t) \tag{5}$$

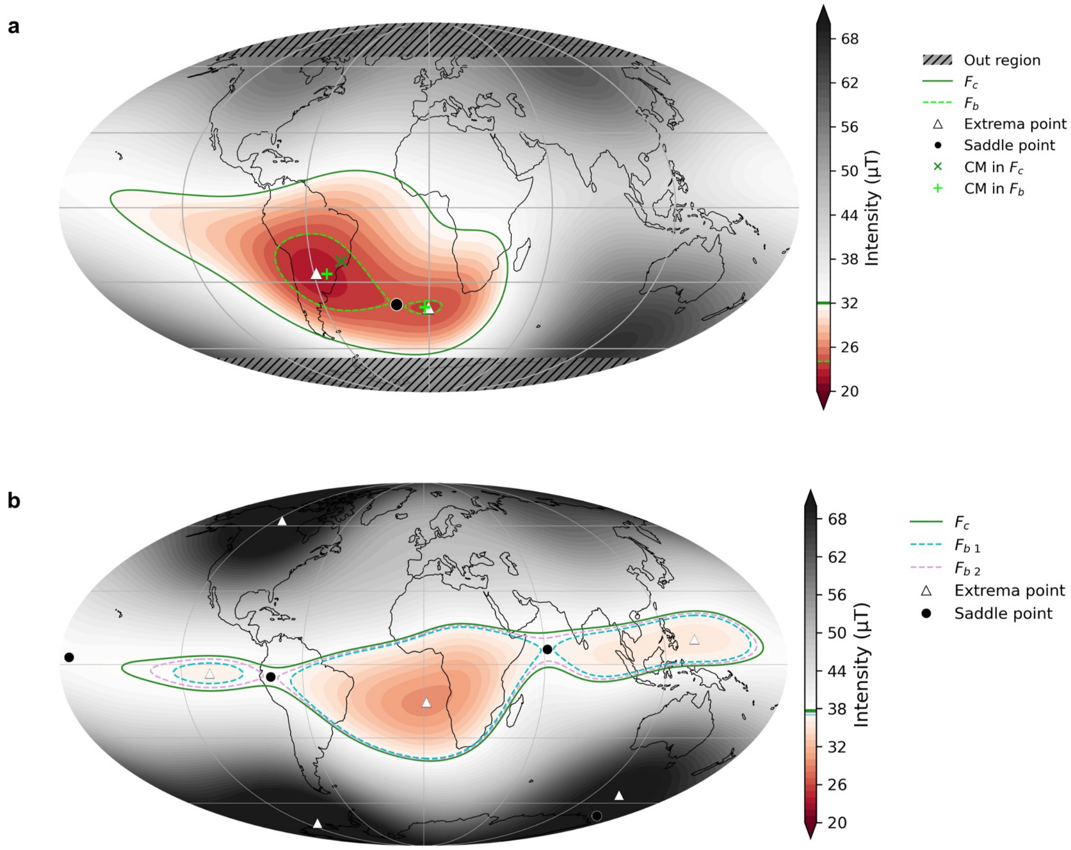


**Figure 2.** (a) Centers and areas of the dual surface intensity minima in 2020 based on CHAOS-8.2. Black shadings indicate the high-latitude regions used to calculate $F_{out}$. The solid green contour outlines the total area of the SAA in 2020. The dashed bright green contours denote the boundaries of sub-regions for each minima determined based on the saddle point intensity (black circle). The center of mass of the total region is marked with a dark green ×, while the centers of mass of the two sub-regions are marked with bright green + symbols. White triangles indicate the locations of the local minima. (b) A complex example from the year 1740 in the HistKalmag model. Two saddle points exist within the total anomaly area. The blue regions correspond to $F_{b1}$ based on the eastern saddle with lower boundary intensity, forming three independent sub-regions. The pink regions correspond to $F_{b2}$ based on the western saddle, forming two independent sub-regions, one of which contains two blue regions.

where the threshold intensity $F_0$ is set to 32 μT. For geomagnetic field models relying on observatory and satellite data for example CHAOS-8.2 (https://www.spacecenter.dk/files/magnetic-models/CHAOS-8) and COV-OBS.x2 (Huder et al., 2020), we adopt 2020 as the reference year, whereas for models that extend to epochs predating the advent of direct intensity measurements (Gauss, 1833), 1950 is selected which corresponds to the last available year of for example model HistKalmag (Schanner et al., 2023).

When the intensity of the global magnetic field is stronger than $F_0$ at a given epoch $t$, the ratio $F_{out}(t) > 1$, resulting in a higher threshold boundary intensity, that is $F_c(t) > F_0$. Our algorithm is therefore not designed to capture past SAA-like features in terms of absolute intensity, but rather in terms of relative intensity and spatial extent. This approach enables a more robust comparison across different global field configurations, including scenarios with substantially different dipole moment strengths.

The total area of the anomaly is defined based on $F_c$ (see solid green contour in Figure 2a). In the absence of a secondary minimum, $F_c$ adequately defines the boundary of a region associated with the global minimum. However, when a secondary minimum is present, it becomes difficult to assign a distinct area to each individual minimum. Using the surface intensity field value at the saddle point $F_{saddle}$, we define boundaries of the distinct sub-regions associated with each minimum as

$$F_b = (1 - \epsilon) \times F_{saddle} \quad (6)$$

where $\epsilon = 10^{-4}$. Because a saddle point serves as a connecting point between two sub-regions containing an extreme point, setting a value slightly below it guarantees their separation. Hence $F_b$ defines sub-region areas $A_{s1}$ and $A_{s2}$ enclosed by directly measured intensity values slightly below and extremely close to $F_{saddle}$. Consequently, two separate contours can be identified, each enclosing exclusively its respective minimum, as shown by the green dashed lines in Figure 2a.

To divide the total area, we normalize the two sub-region areas $\frac{A_{s_1}}{A_{s_1}+A_{s_2}}$ and $\frac{A_{s_2}}{A_{s_1}+A_{s_2}}$. These fractions are then multiplied by the total area, thereby partitioning it into two distinct scaled effective areas $A_1$ and $A_2$ associated with their respective minima:

$$A_1 = A_{total} \cdot \frac{A_{s_1}}{A_{s_1} + A_{s_2}}, \quad A_2 = A_{total} \cdot \frac{A_{s_2}}{A_{s_1} + A_{s_2}} \tag{7}$$

Next, following Amit et al. (2021), the CM of each anomaly region (region/sub-regions corresponding to single/multiple anomaly scenarios) is calculated to provide a representative geographic position weighted by the inverse of the field intensity.

$$\phi_{CM} = \frac{\sum_i \phi_i w_i \sin\theta_i}{\sum_i w_i \sin\theta_i}, \tag{8}$$

$$\theta_{CM} = \frac{\sum_i \theta_i w_i \sin\theta_i}{\sum_i w_i \sin\theta_i}. \tag{9}$$

The $\phi_{CM}$ and $\theta_{CM}$ are the longitude and co-latitude of the CM, respectively. The weighting factor for each point is defined as

$$w_i = \frac{1}{F_i}, \tag{10}$$

where $\theta_i$ and $\phi_i$ denote the co-latitude and longitude of the $i$ point, respectively. The CM of the entire anomaly is calculated over the area enclosed by $F_c$ (solid green contour in Figure 2a), whereas the centers of mass of the sub-regions (if they exist) are calculated using $F_b$ (dashed green contours in Figure 2a).

So far, we described a configuration in which the $F_c$ area has been divided into two sub-region areas. However, during the historical era, the situation at some specific snapshots is more complex, with multiple saddle points producing multi-level nested sub-regions. Although the principle of dividing sub-regions by saddle point intensity remains valid, the procedure becomes more intricate. To address this complexity, we adopt a hierarchical approach, partitioning the total area step by step from the innermost to the outermost boundaries. In this way, the complex problem is reduced to the simplest case, where the enclosed sub-regions are used to divide the surrounding area into corresponding fractions.

Figure 2b shows a typical complex case with multiple saddle points and nested sub-regions. In Figure 2b, the dashed blue contours define three inner sub-regions, while the dashed pink contours represent two broader areas: one on the west that encompasses one minimum and another on the east that encloses two of the blue sub-regions. Within the eastern pink contour, the fractional areas of the inner blue sub-regions are first calculated. The enclosed pink region is then subdivided proportionally, following Equations 6 and 7. At this stage, the area within the right pink contour has been divided into two parts by the inner blue regions. Then combined with the isolated western pink area, this results in three distinct fractions, each corresponding to a different minimum. These three fractional areas are then used to partition the next outer contour—in this case, $F_c$. If the outer boundary corresponds to another $F_b$, the same hierarchical procedure is applied iteratively until the outermost contour $F_c$ is reached.

The procedure is summarized as follows: first, identify the saddle points within the $F_c$ region; then rank them in ascending order of intensity; next, construct the corresponding $F_b$ contours; and finally, partition the area

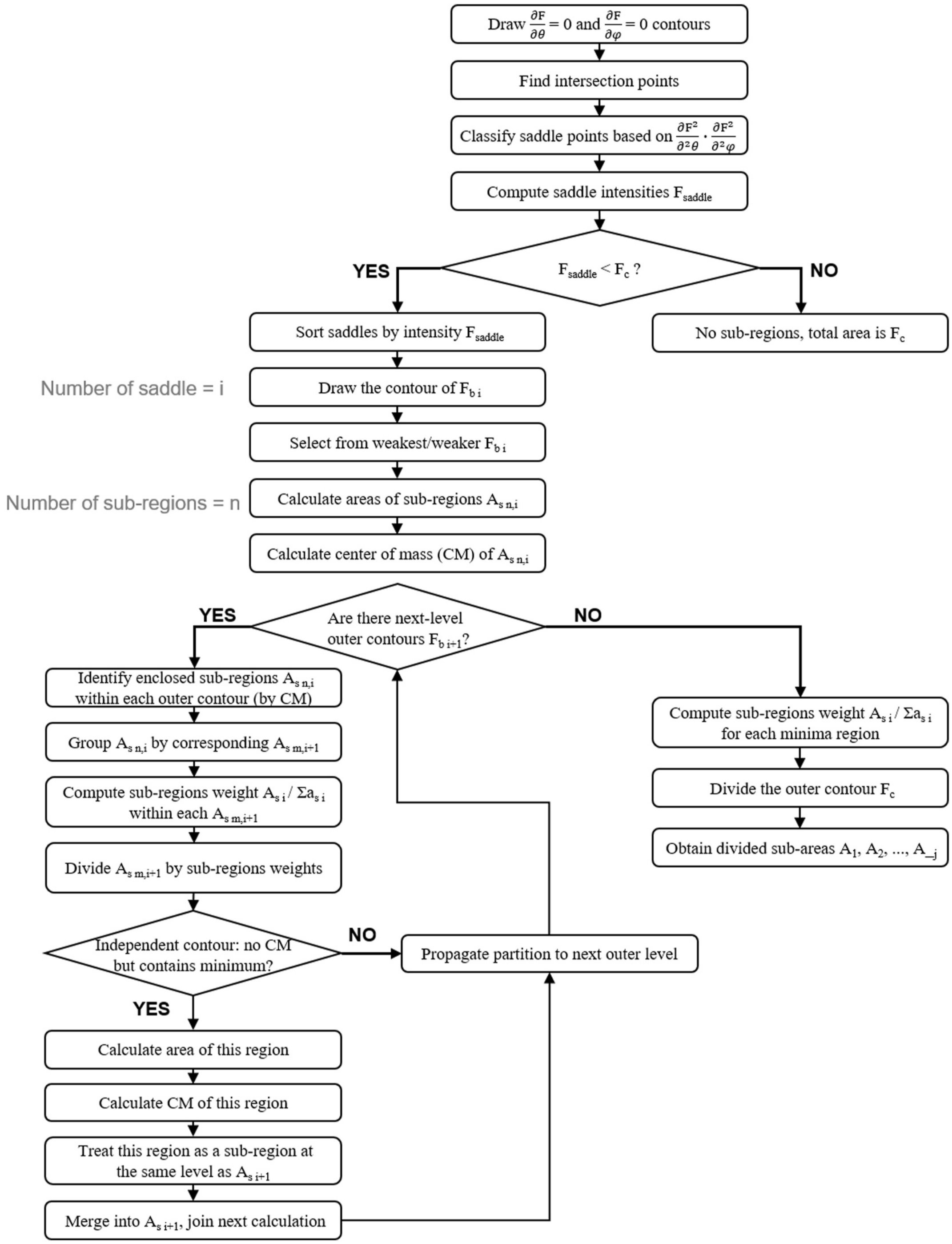


**Figure 3.** Flowchart of the method used to identify and divide geomagnetic anomaly sub-regions. Saddle points are first identified. If saddle points exist within the $F_c$ contour, the enclosed regions are progressively partitioned from inner to outer contour levels into multiple sub-regions according to their relative area proportions. The procedure is repeated for higher contour levels until the outer contour $F_c$ is completely divided. The final partitioned sub-regions are denoted as $A_1, A_2, \ldots, A_j$.

hierarchically from the innermost to the outermost boundary. The complete description is provided in a flowchart in Figure 3.

The CM serves as a key criterion to determine whether a sub-region belongs to a specific upper-level region in a nested structure. In a few rare snapshots, several minima fall within a single $F_b$ contour (see Movie S3). Because these minima are nearly identical in both intensity and location, we treat them as one combined minimum, whose position is represented by the CM of the enclosed sub-region. This recursive approach of our topological algorithm allows for any number of sub-regions to be assigned hence it can be applied to much more spatially complex fields, as for example, the outputs of numerical dynamo simulations that typically contain much smaller spatial scales than field models based on observables.

### 2.3. Null Intensity Gradient Contours

In addition, we analyzed the distribution of the $\frac{\partial F}{\partial \theta} = 0$ and $\frac{\partial F}{\partial \phi} = 0$ contours. In particular, we focused on the spatial characteristics of $\frac{\partial F}{\partial \theta} = 0$ near the equator. These distributions may be compared with an idealized purely axial dipole field in which $\frac{\partial F}{\partial \theta} = 0$ coincides with the geographic equator and $\frac{\partial F}{\partial \phi} = 0$ holds everywhere on the spherical surface.

For each year, the $\frac{\partial F}{\partial \theta} = 0$ contour near the equator was analyzed. The northernmost, southernmost and mean latitudes of this contour were recorded to describe its overall north-south position. To examine longitudinal variation, the globe was divided into 5° longitude bins. In each bin, the latitudinal difference between the northernmost and southernmost points on the contours in all years was determined to reflect the extent of variation across different longitudes.

The spatial and temporal distributions of $\frac{\partial F}{\partial \phi} = 0$ were also analyzed. The number of points along the $\frac{\partial F}{\partial \phi} = 0$ contours falling within each 5° longitude bin was counted over time to show the longitudinal density of these contours.

## 3. Results

The HistKalmag model, which combines historical ship log archieves and archeomagnetic data, is used to calculate the time dependence of surface intensity anomalies between 1000 and 1950 CE. The CHAOS-8.2 model, based on magnetic field observations from low-Earth orbit satellites and annual differences of monthly means from ground observatories, is used for the period 2000 to 2024 CE to describe the recent temporal dependence of the SAA. The COV-OBS.x2 model, primarily constrained by observatory time series, satellite data and historical ship log archieves, covers the period 1840 to 2020 hence it is employed to bridge the intermediate period between CHAOS-8.2 and HistKalmag.

### 3.1. Extrema and Saddle Points

Figure 4a shows the geomagnetic surface intensity in 2020 based on the modern field model CHAOS-8.2. The null contours of $\frac{\partial F}{\partial \theta} = 0$ (black solid lines) and $\frac{\partial F}{\partial \phi} = 0$ (black dashed lines) intersect at extrema and saddle points. In the $\frac{\partial^2 F}{\partial \theta^2} \cdot \frac{\partial^2 F}{\partial \phi^2}$ map (Figure 4b), depending on whether these products are positive or negative, we identify extrema or saddle points respectively.

Each saddle point is located between two extrema. Within the SAA region (the area inside the green line in Figure 4a), the saddle appears between two minima. Outside the SAA area, the saddle in South Asia is located between two high-latitude maxima, while the saddle in Alaska is between two maxima near the North Pole.

### 3.2. Satellite Era Split of the SAA

Figure 5 shows the time dependence of the SAA from 2000 to 2020 CE. For the entire period, a large southward bulge characterizes the low-latitude $\frac{\partial F}{\partial \theta} = 0$ contour. The temporal change of the $\frac{\partial F}{\partial \theta} = 0$ contour is relatively small during this period. However, the $\frac{\partial F}{\partial \phi} = 0$ contour through the SAA exhibited significant temporal variation in the Southern Hemisphere. In 2000 and 2005, the $\frac{\partial F}{\partial \phi} = 0$ contour presents an east–west orientation in the South Atlantic; consequently, it intersects the $\frac{\partial F}{\partial \theta} = 0$ contour only in South America (Figures 5a and 5b). In contrast, in 2010 and 2020, the $\frac{\partial F}{\partial \phi} = 0$ contour shows a southwest-to-northeast orientation in the South Atlantic (Figures 5c and 5d), leading to the emergence of a new local minimum near South Africa. The $\frac{\partial F}{\partial \phi} = 0$ contour in the Atlantic further advanced northward in 2020, causing the saddle to gradually drift from a location near the South Africa minimum (Figure 5) to a more westerly location. Overall in these 20 years, the $\frac{\partial F}{\partial \theta} = 0$ contour, which crosses the

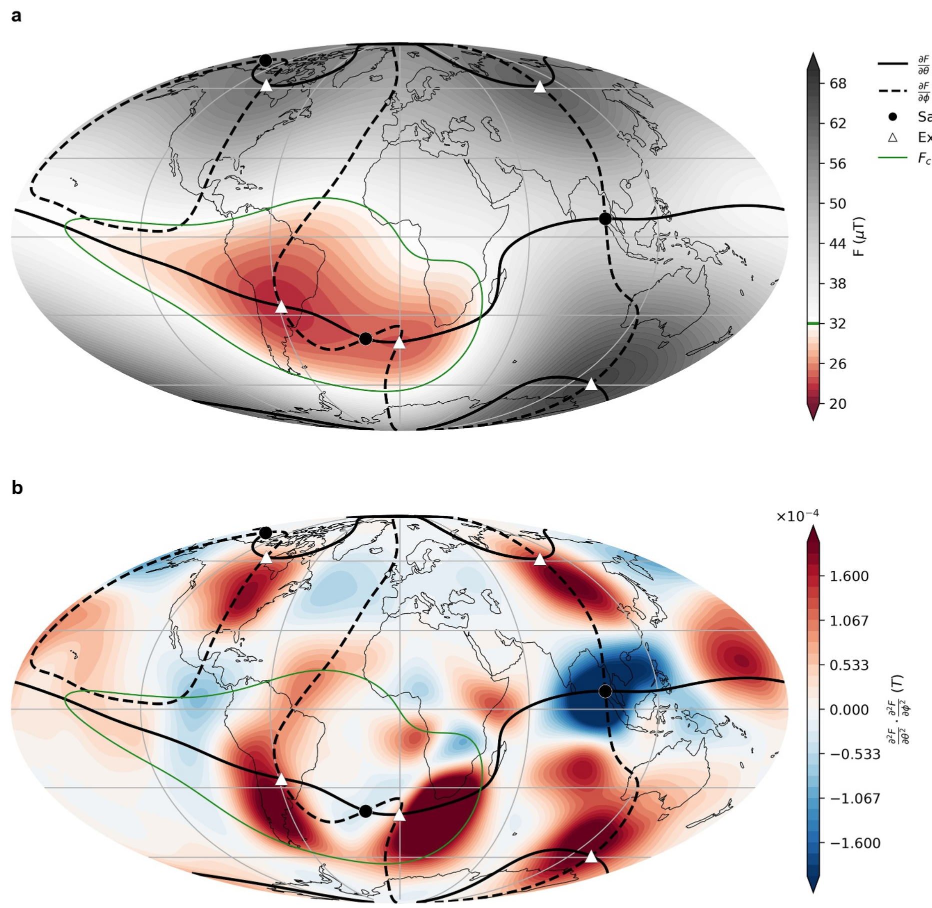


**Figure 4.** (a) Geomagnetic surface intensity and (b) $\frac{\partial^2 F}{\partial \theta^2} \cdot \frac{\partial^2 F}{\partial \phi^2}$ in 2020 based on CHAOS-8.2. The solid black lines represent $\frac{\partial F}{\partial \theta} = 0$, the dashed black lines represent $\frac{\partial F}{\partial \phi} = 0$. White triangles mark the extrema (both maxima and minima), black circles denote saddle points between the extrema. Extrema are located in regions with positive values (red), while saddle points lie in regions with negative values (blue).

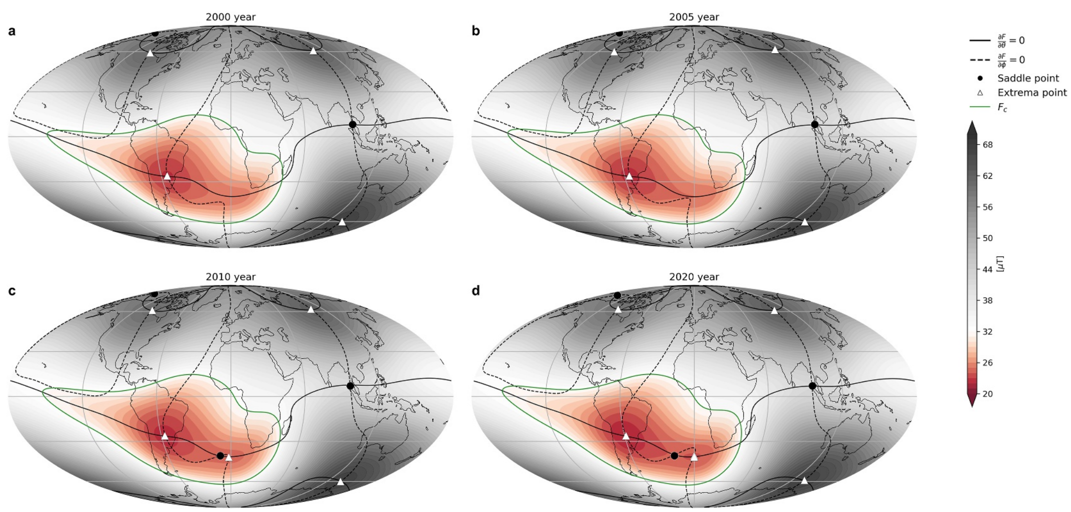


**Figure 5.** Snapshots describing the recent SAA transition from a single surface intensity minimum to a pair of minima.

10.1029/2026JB033955

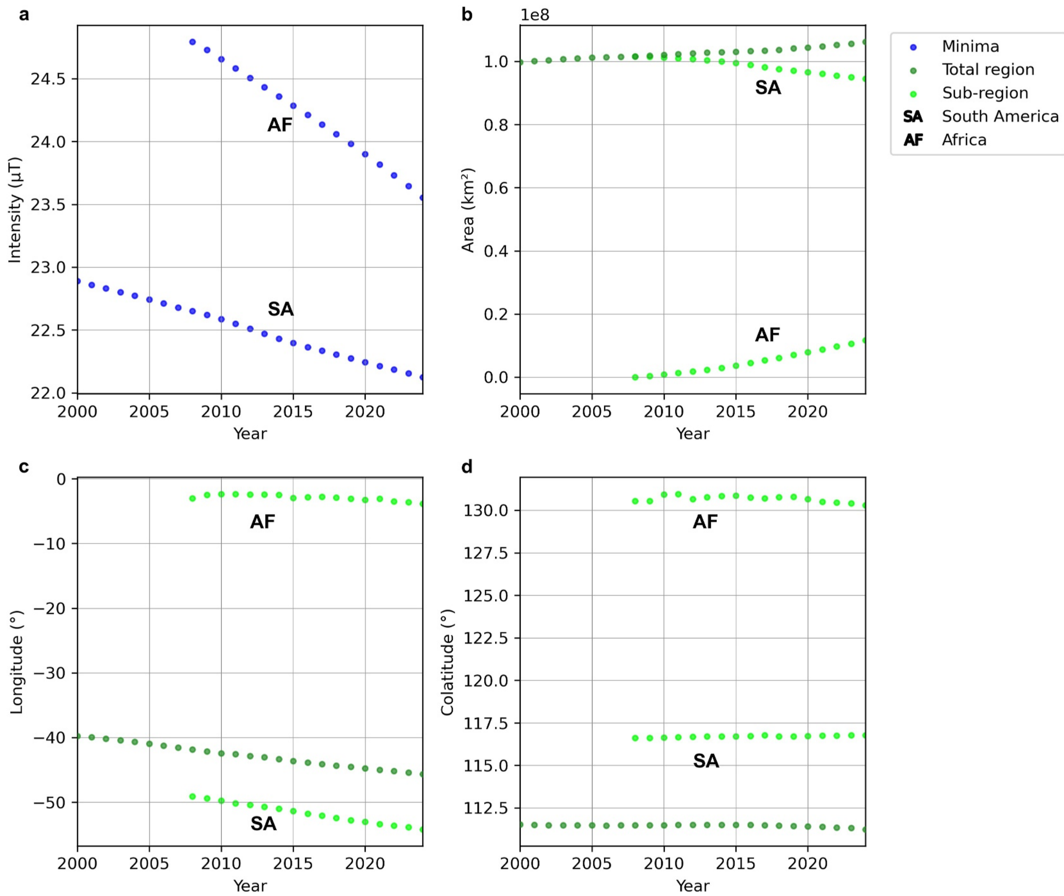


**Figure 6.** (a) SAA local minima intensity, (b) total and areas of the sub-regions, (c) longitude and (d) co-latitude of the centers of mass of the sub-regions based on CHAOS-8.2 model. Blue in (a) indicate minima; In (b) the dark green represents the area of the total SAA region, the bright green denote the areas of sub-regions defined by the saddle points. The sum of the two sub-region areas equals the total area. In (c) and (d) the dark green denote the centers of mass of the total SAA region, and the bright green denote the centers of mass of the sub-regions whenever a secondary minimum appears. Letter markers indicate the geographic locations of the sub-regions.

equator in the Pacific and Indian Oceans, shifted markedly southward far from the equator in the South Atlantic region, and did not experience significant changes.

### 3.3. Areas and Centers Time Dependence

The time dependence of the recent SAA areas and centers based on the CHAOS-8.2 geomagnetic field model is shown in Figure 6 (see Movie S1 for all snapshots). Since the SAA split into two parts only after 2008, a pair of minima at two sub-regions appear in Figure 6 from that year onward.

Figure 6a shows that the intensities of the South America ("SA" in Figure 6) and South Africa ("AF" in Figure 6) minima have been decreasing rapidly. However, the rate of decrease in South Africa is significantly faster. According to corresponding linear fits, the South America minimum weakened at a rate of approximately 33 nT $yr^{-1}$, while the South Africa minimum decreased at a rate of about 77 nT $yr^{-1}$ (Table 1), more than twice faster!

Figure 6b shows that the total SAA area (dark green, $A_{total}$) has been increasing at a rate of $2.4 \times 10^5$ $km^2$ $yr^{-1}$ (Table 1). A closer examination of the SAA through its individual sub-regions (bright green, $A_1$ and $A_2$) interestingly reveals that the area of the weaker primary minimum has actually been shrinking, whereas that of the secondary minimum has been rapidly expanding.

The expansion of the South Africa minimum (Figure 6b) is obviously related to the faster decrease in its intensity (Figure 6a). However, the shrinkage of the South America area is not trivial. Since 2008, when the split occurred,

**Table 1**
*Rates of Change of Geomagnetic Surface Intensity Minima Characteristics Based on the COV-OBS.x2 and CHAOS-8.2 Models*

| Model | COV-OBS.x2 | | | | CHAOS-8.2 | |
|---|---|---|---|---|---|---|
| Total region | | | | | | |
| Period | 1840–2024 | | | | 2000–2024 | |
| Global min intensity (nT/yr) | −29.80 | | | | −32.68 | |
| Area ($10^6$ km$^2$/yr) | 0.24 | | | | 0.24 | |
| CM longitude (°/yr) | −0.13 | | | | −0.25 | |
| CM colatitude (°/yr) | 0.05 | | | | −0.01 | |
| Sub-regions | | | | | | |
| Period | 1866–1928 | | 2012–2024 | | 2008–2024 | |
| Location | South America | Pacific | South America | South Africa | South America | South Africa |
| Intensity (nT/yr) | −30.74 | −20.13 | −32.6 | −79.35 | −33.06 | −76.95 |
| Area ($10^6$ km$^2$/yr) | 0.14 | 0.01 | −0.67 | 0.93 | −0.48 | 0.74 |
| CM longitude (°/yr) | −0.24 | 0.19 | −0.33 | −0.17 | −0.32 | −0.08 |
| CM colatitude (°/yr) | 0.02 | 0.01 | 0.01 | −0.03 | 0.01 | −0.02 |

*Note.* Obtained by linear fits of the results shown in Figures 6 and 7. CM denotes center of mass.

the area of the primary minimum decreased by $4.8 \times 10^5$ km$^2$ yr$^{-1}$, while that of the secondary minimum increased by $7.4 \times 10^5$ km$^2$ yr$^{-1}$ (Table 1).

The CM of the total area drifted westward at a rate of 0.25° yr$^{-1}$ and northward at a nearly zero rate of about 0.01° yr$^{-1}$ (see dark green in Figures 6c and 6d). The CM of the primary minimum drifted westward at a slightly faster rate of 0.32° yr$^{-1}$ (see bright green in Figure 6c). In contrast, the CM of the secondary minimum exhibited smaller changes in longitude (bright green signs in Figure 6c). Both minima exhibited practically no latitude changes (see bright green signs in Figure 6d and Table 1).

The results based on the analysis of the COV-OBS.x2 model include the period covered by the CHAOS-8.2 model with the most recent split of the SAA (see Movie S2 for all snapshots). For the most recent times, results of Figure 7 are thus qualitatively similar to Figure 6. However, the expansion of the South Africa minimum and the shrinkage of the South America minimum are more pronounced based on COV-OBS.x2 (Figure 7b and Table 1). In addition according to the COV-OBS.x2 model, the South Africa minimum exhibits a significantly faster westward drift than in CHAOS-8.2 (Table 1).

Another minimum appears in Figure 7 between 1866 and 1928. Distinct from a split of the SAA region, it represents the emergence of a new, independent anomaly located over the Pacific Ocean, clearly separated from the main SAA area. It could be a recurrent event of the WPA (Yue et al., 2024). This independently emerged minimum did not significantly affect the evolution of the primary SAA area. It was characterized by a relatively high intensity (∼35 μT, see Figure 7a) and a consistently small area (less than $1.6 \times 10^6$ km$^2$, see Figure 7b). It exhibited no significant expansion, and it gradually drifted eastward toward the main SAA region.

The results from the HistKalmag model (Figure 8) reveal a longer-term hence more complex evolution (see Movie S3 for all snapshots of the mean model). The intensities of the minima indicate that the current SAA began to weaken around 1770 (Figure 8a). However, over the past thousand years, the minima did not always weaken as rapidly as they do today; e.g., during the period from 1500 to 1750, their intensities changed very little. The secondary minimum observed between 1866 and 1928 is not captured by this smoother model.

The time dependence of the minima involves splitting, emergence and disappearance, similar to the surface intensity minima cycle found by Yue et al. (2024). Split events exhibit pronounced anti-correlation in area variations (e.g., 1040–1200; Figure 8b), whereas emerged events have little effect on the evolution rates of other contemporaneous sub-regions, primarily influencing the total area (e.g., 1400–1600). Alternating events of total area expansion or shrinkage are evident in the historical record, with typical timescales of about 150 years (Figure 8b).

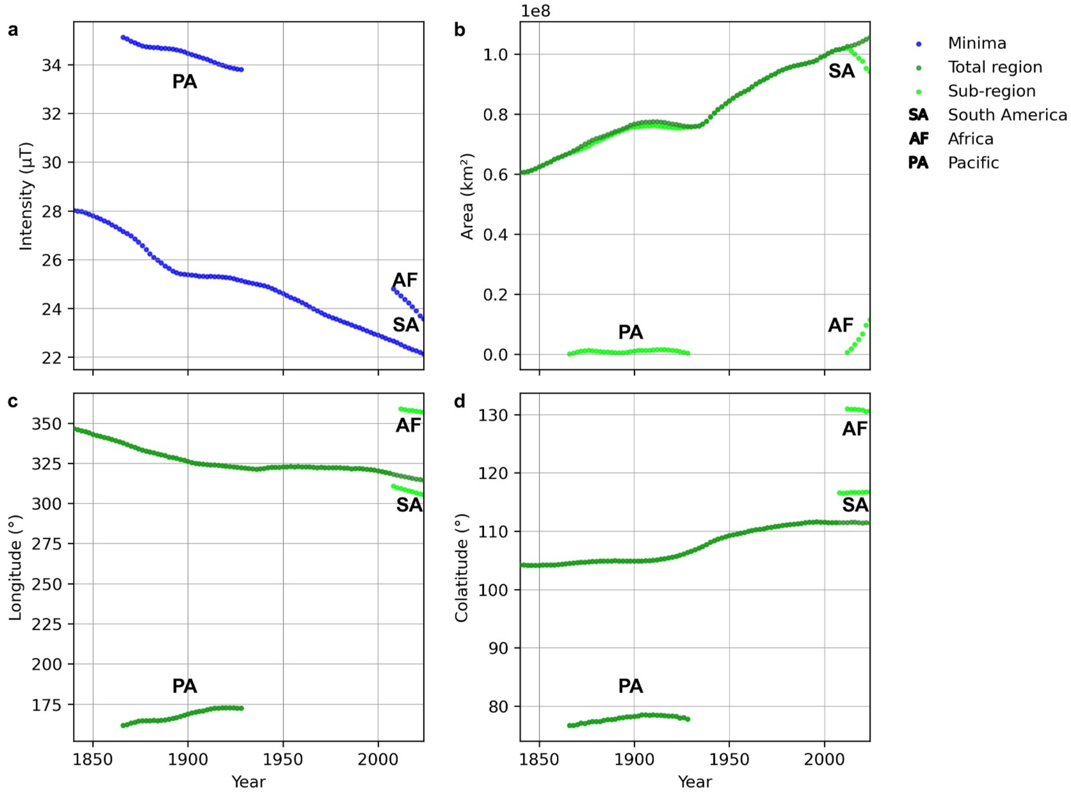


**Figure 7.** As in Figure 6 for the COV-OBS.x2 model.

Figures 8c and 8d show the temporal evolution of the longitude and latitude of the centers of mass for both the total area and the sub-regions. Over the longer periods covered by this model, both westward and eastward drifts are observed. In addition, larger latitudinal changes are found (Figure 8d) compared to the recent SAA. However, Figure 8d shows that the CM in HistKalmag model has never reached the high latitude currently observed for the South African minimum (approximately 40°S; see Figure 6d).

The period from 1700 to 1820 represents a particularly chaotic phase, during which the total area decreased substantially and multiple sub-regions coexisted, with up to four coexisting at a given time. The rareness of this chaotic phase may suggest that surface intensity minima in the west Pacific are not persistent. However, recurrent WPAs were reported in the other archeomagnetic field models (Tema et al., 2023).

In order to evaluate the impact of the uncertainty in archeomagnetic field models on our results, we further analyzed 50 realizations of the HistKalmag model, shown in pale colors in Figure 8. For all quantities, that is intensity, area and centers, the realizations strongly converge after 1550, whereas larger dispersion is observed before 1550. The uncertainty seems smaller for the location than for the intensity and area. Nevertheless, the results remain clustered around the mean trend, supporting the robustness of the main results.

### 3.4. Null Intensity Gradient Contours

#### 3.4.1. Hemispheric Asymmetry in $\frac{\partial F}{\partial \theta} = 0$ Contours

For a purely axial dipolar geomagnetic field, the $\frac{\partial F}{\partial \theta} = 0$ contour coincides with the geographical equator. The distribution of the null contours and in particular their deviation from the equator therefore reflects non-dipole features. Here, we present the historical distribution of $\frac{\partial F}{\partial \theta} = 0$ contours.

Figures 9a and 9b show the distribution of the $\frac{\partial F}{\partial \theta} = 0$ contours from 1000 to 2020 CE. In general, three main groups of contours can be identified: two located near the geographical poles and another at low latitudes crossing the equator. An additional closed contour occasionally appears at mid-to-low latitudes, for example, in Figure 9a

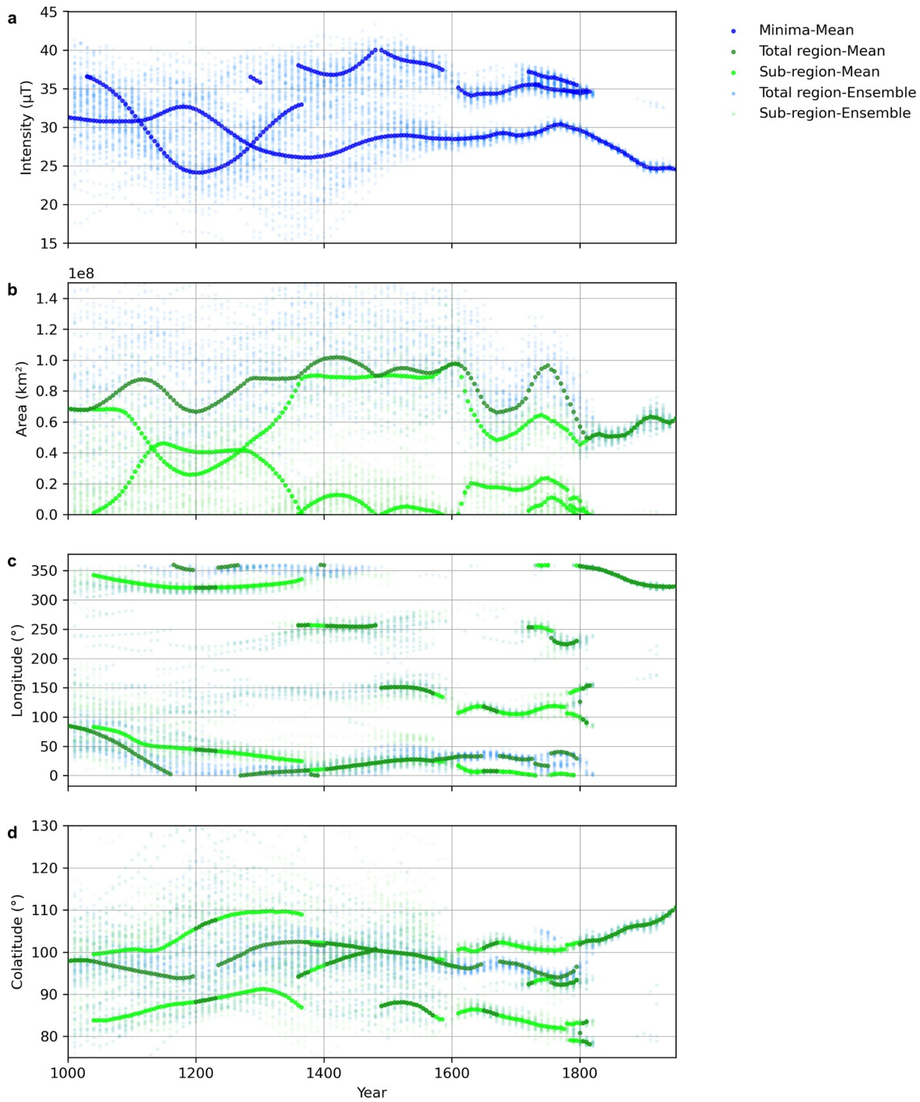


**Figure 8.** As in Figure 6 for the HistKalmag model.

over the Indian Ocean and in Figure 9b over southeastern Africa, sometimes connecting to the equatorial branch. We focus on the low-latitude group of $\frac{\partial F}{\partial \theta} = 0$ contours which is relevant for surface intensity minima.

The latitudinal width of the equator-crossing contours varies with longitude, as shown in Figures 9c and 9d. The width in the Atlantic hemisphere is larger than in the Pacific hemisphere, reaching 40–50° (Figures 9a and 9b). Minimal widths occur over the Pacific, with strong convergence near 140°E. In the period 1840 to 2020 CE, this contour spreads widely in the SAA region, with the most pronounced peak in width located near South Africa at around 30°E (Figures 9b and 9d). This change around 1840 is either due to the improved data in the COV-OBS.x2 model or it represents a genuine change in the spatial distribution of the field in the past two centuries.

In addition, the $\frac{\partial F}{\partial \theta} = 0$ contours also exhibit a pronounced southward tendency. The strongest southward intrusions occurred between 1200 and 1400 CE and from 1930 to the present, as indicated in Figures 9e and 9f by co-latitude 135°, that is maximum latitude of 45°S. In contrast, the Northern Hemisphere maxima are at co-latitude 75°, that is maximum latitude of 15°N (blue curves). Moreover, the mean co-latitude of the $\frac{\partial F}{\partial \theta} = 0$ contours (green curves) is systematically greater than 90°, indicating the tendency toward the Southern Hemisphere.

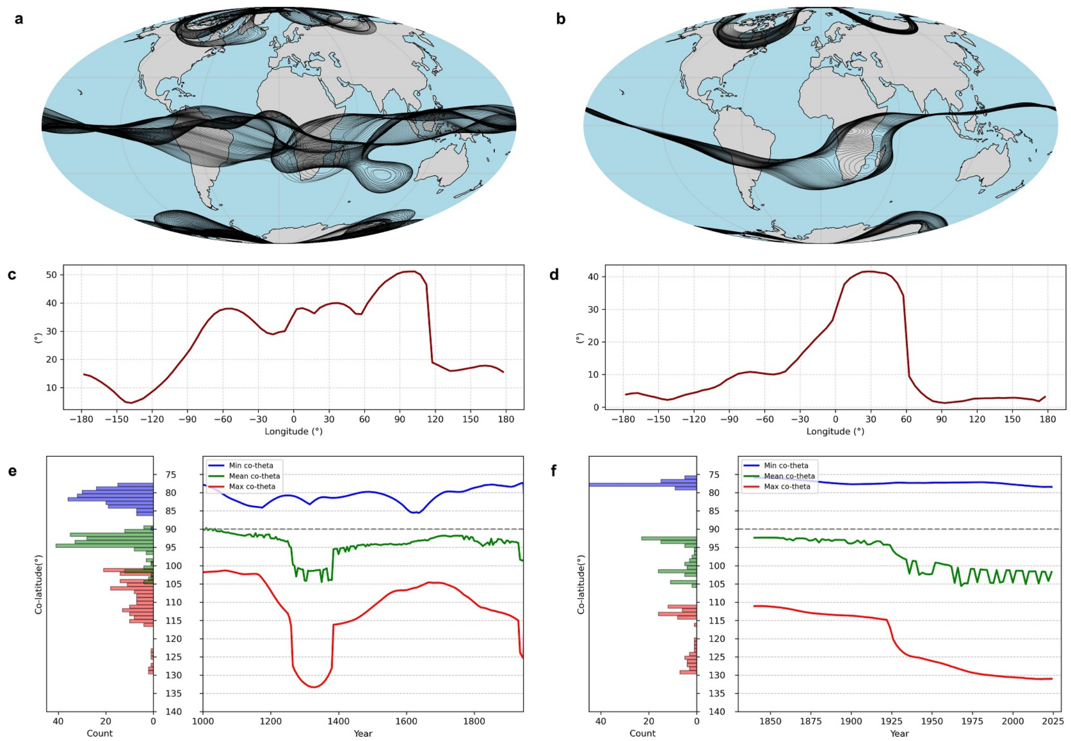

**Figure 9.** Distribution of all $\frac{\partial F}{\partial \theta} = 0$ contours from 1000 to 1950 CE by the HistKalmag model (a) and from 1840 to 2020 CE by the COV-OBS.x2 model (b), shown as black lines. Panels (c) and (d) show the width of the null contour distribution crossing the equator. Panels (e) and (f) display the maximum, minimum, and average co-latitude values of the contour lines at low latitudes (20–50°). In these two panels the histograms share the same $y$-axis (co-latitude) with the line plots. The histograms on the left summarize the number of extreme and mean values of the contour lines at each latitude for all years, with colors corresponding to the solid lines shown in the right-hand subplots.

### 3.4.2. Distribution of $\frac{\partial F}{\partial \phi} = 0$ Contours

Next we analyze $\frac{\partial F}{\partial \phi} = 0$ contours, which are also required to obtain a surface intensity minimum. In a pure axial dipole field, $\frac{\partial F}{\partial \phi} = 0$ contours should occur everywhere. However, from 1000 to 1950 CE in the HistKalmag model, two void regions one over Brazil and another over the southern Indian Ocean appear (Figure 10a), possibly suggesting that the present location of the SAA in Brazil is rare. Alternatively, even the millennial scale

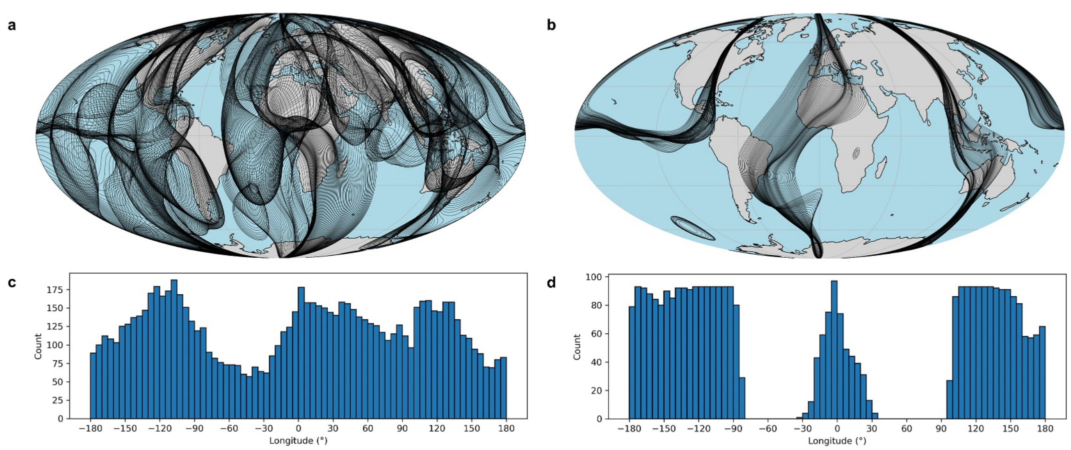

**Figure 10.** Distribution of all $\frac{\partial F}{\partial \phi} = 0$ contours, (a) from 1000 to 1950 with HistKalmag model and (b) from 1840 to 2020 with COV-OBS.x2. (c) and (d) Distribution of the contour along longitude. Each bin represents 10° of longitude.

HistKalmag model might not represent the long term behavior of the geodynamo (Terra-Nova et al., 2019). The two voids in Figure 10a are further demonstrated by the longitude distribution in Figure 10c, which shows pronounced minima at these locations. Over the short recent period in Figure 10b, a northeastward protrusion of the contours in the South Atlantic is associated with the emergence of the secondary minimum. The $\frac{\partial F}{\partial \phi} = 0$ contours over the Pacific barely reach the Southern Hemisphere.

## 4. Discussion

In this paper we introduce a new topological algorithm to systematically characterize multiple geomagnetic surface intensity minima using saddle points between pairs of minima. The algorithm uniquely determines for the first time the enclosed sub-regions associated with each minimum, thereby enabling a quantitative partitioning of the total anomaly area into distinct parts associated with each minimum. The boundaries of these sub-regions evolve with the variation of saddle points, leading to time-dependent sub-region boundaries that adapt to changes in the field. This algorithm was applied to the CHAOS-8.2, COV-OBS.x2 and HistKalmag geomagnetic field models to investigate the temporal evolution of geomagnetic surface intensity anomalies over decadal, centennial and millennial timescales. As a result, it successfully captures the recent rapid area changes in the two SAA sub-regions (Figure 6). Apart from the recent split we also found surface intensity minima emerging at other locations away from the SAA (Figure 7). Analysis of a longer time field model reveals a recurrent expansion and shrinking of pairs of surface intensity minima that resulted in splits (Figure 8), which resemble the field behavior at present (Figure 6). In addition, the distribution of null intensity gradient contours reveals hemispheric asymmetry in the contribution of non-dipole field to the location of surface intensity minima.

In our algorithm, the intensity threshold is factored by a time-dependent ratio $F_{\mathrm{out}}$, derived from averaging strong magnetic intensity at high latitudes outside the SAA. This effectively reduces the influence of global field changes on the assessment of regional anomalies. This approach is similar to that of Amit et al. (2021) and Yue et al. (2024), although the selection of the $F_{\mathrm{out}}$ region differs because in the longer periods explored in this study the surface intensity anomalies cover larger regions which should be avoided by $F_{out}$. Nevertheless, our resulting trend of anomaly is similar to that reported by Amit et al. (2021). Accounting for $F_{\mathrm{out}}$ reduces the rate of change of area because the intensity at high latitudes also rapidly changes (Livermore et al., 2020). The SAA expansion rate we calculated using $F_{\mathrm{out}}$ is thus lower than the expansion rates reported by Finlay et al. (2025).

The method for defining the areas of sub-regions enables the calculation of area changes associated with each individual minimum. The saddle-point intensity varies with the evolution of the two local minima, providing a dynamic threshold that adapts to temporal changes in the geomagnetic field. This adaptive threshold defines the largest critical intensity that preserves the independence of the two local minima sub-regions. In contrast, a fixed-threshold approach cannot consistently maintain the separation of the two minima over time since the two sub-regions can only be identified when the threshold lies right between the intensity of the less weak minimum and $F_{saddle}$. This makes it practically impossible to identify multiple surface intensity minima associated with sub-regions over long periods using a fixed threshold. Moreover, choice of the fixed threshold value might lead to distinctive estimates of the SAA area expansion rate. In Finlay et al. (2025), the total SAA area enclosed by the 24 μT contour grows much faster than areas enclosed by contours of other intensities. This value approximately corresponds to the intensity at the saddle point which is used to define the sub-regions (green dashed line in Figure 2a); for example, in 2020, $F_b = 23.8$ μT. Thus, a threshold intensity close to the saddle intensity value highlights the growth of the Africa minimum. Our algorithm well captures the recent rapid variations in the areas of the two sub-regions within the SAA, especially the newly emerging and rapidly expanding local minimum region in southwest of Africa.

Our algorithm relies on the analysis of null intensity gradient contours, providing new insights into the temporal variations of the SAA. Over the past 20 years, the rapid changes within the SAA are primarily caused by changes in the $\frac{\partial F}{\partial \phi} = 0$ contour in the southeast region. These rapid changes led to the emergence of the new Africa minimum (Figure 5). In addition, we note that the two null intensity gradient contours in equatorial Pacific are parallel and close to each other (Figure 5). This implies a higher probability that a new minimum may emerge in this region in the near future.

Analysis of the HistKalmag geomagnetic field model suggests that the recent expansion and intensity decrease of the SAA may have begun as early as 1780 (Figure 8). For most of the past 240 years, the SAA has maintained

10.1029/2026JB033955

several persistent characteristics: decreasing intensity, expansion, westward drift and a weak southward drift. During this period, based on the analysis of the COV-OBS.x2 model, two distinct modes of local minimum formation were identified. The first type is an emergence event: between 1860 and 1930, a small isolated minimum appeared over the Pacific, exerting very little (if any) influence on the main (i.e., the weakest) anomaly (Figure 7). The second type is a splitting process, in which a new local minimum develops through the division of the existing anomaly. Around 2008, based on both COV-OBS.x2 and CHAOS-8.2 models, such a split has occurred, producing a pair of minima within the same SAA region (Figures 6 and 7). In contrast to the emergence case, splitting has a significant impact on the evolution of the SAA, particularly in total as well as the area of sub-regions change.

The recent splitting event is especially noteworthy. The intensity of the new local minimum has been decreasing at twice the rate of the primary minimum (Figure 6a), faster than historical decline rates (Amit et al., 2021; Pavón-Carrasco & De Santis, 2016). The total anomaly area continues to expand during this interval, while the sub-regions exhibit an anti-correlation: the area of the South America minimum is shrinking, whereas the area of the new Africa minimum is rapidly growing (Figure 6b). The time dependencies of the coordinates of the corresponding centers of mass further reveal different behaviors, with both minima drifting westward, but the South American minimum drifts approximately four times faster (Figure 6c). If this trend persists, the two centers of the minima will continue to drift apart within the SAA. Finally, the latitude of the CM of the total area is consistently located farther north than that of either sub-regions (Figure 6d), reflecting the asymmetric shape of the SAA, in particular its northern bulge (Figure 2a).

The analysis of the HistKalmag model suggests that the present-day SAA is not unique (Figure 8). Over the HistKalmag period, the mean number of local intensity minima per snapshot is 2.01, which is comparable to albeit slightly lower than the statistics reported for other archeomagnetic field models (see Terra-Nova et al., 2019). As shown in Figure 8b, multiple sub-regions are present during most of the model period. Several periods exhibit anti-correlated expansion and shrinkage of the area of sub-region caused by split, most notably during 1030–1380 and 1600–1700 CE. The total area has undergone multiple phases of expansion, each with a rate roughly comparable to the modern SAA expansion rate. These episodes of total anomaly area expansion typically last $\sim 150$ years, consistent with the advection time in the core (Terra-Nova & Amit, 2020), suggesting that the expansion of weak geomagnetic surface intensity anomalies is linked to transport processes by fluid flow at the top of Earth's core. The CM of the total anomaly area exhibits both westward and eastward drifts (Figure 8c). Before 1200 CE, the motion resembles the westward drift observed during the last two centuries (Amit et al., 2021; Aubert, 2015) as well as in some archeomagnetic field models (Hellio & Gillet, 2018; Nilsson et al., 2020). Between 1200 and 1600 CE, however, the CM of the total area showed a relatively slow but persistent eastward drift. The sub-regions also display both westward and eastward motions (Figure 8c), consistent with the behavior of intense core mantle boundary (CMB) flux patches in other archeomagnetic field models (Amit et al., 2011; Dumberry & Finlay, 2007; Terra-Nova et al., 2015, 2016).

Despite these historical similarities, the modern SAA remains a particularly noteworthy case. Although the recent global minimum is not decreasing at the fastest historical rate, its intensity is the lowest ever directly observed—since the advent of geomagnetic intensity measurements by Gauss nearly 200 years ago, the surface intensity never dropped below 23 μT. Likewise, although north–south migration of anomalies has occurred before, the present SAA has reached the lowest southern latitude recorded in the historical models, a feature that seems challenging to reproduce in numerical dynamo simulations (Terra-Nova & Amit, 2025).

We further performed an analysis of the distribution of null intensity gradient contours which has the advantage of not requiring any arbitrary choice of intensity threshold. Our analysis reveals hemispheric asymmetry in non-dipolar features. In Figures 9e and 9f, the maximum deviation of the $\frac{\partial F}{\partial \theta} = 0$ contours from the equator shows that non-dipolar features associated with surface intensity anomalies are clearly more pronounced in the Southern Hemisphere than in the Northern. Similar north-south asymmetry was reported in previous studies based on archeomagnetic field models bearing in mind the possible bias due to eneven spaial distribution of the data (Constable et al., 2016; Constable & Parker, 1988; Gallet et al., 2009; Nilsson et al., 2022, 2024). This long-term hemispheric preference, emerging over millennial timescales, may be linked to the southern locations of the LLSVPs (Lézin et al., 2023), which control the CMB heat flux and hence the spatial pattern of core convection and the geomagnetic field (Amit et al., 2015). Alternatively, the north-south dichotomy may simply be the outcome of the uneven spatial distribution of archeomagnetic data. Furthermore, in Figures 9c and 9d, the broader distribution of $\frac{\partial F}{\partial \theta} = 0$ contours in the Atlantic hemisphere, together with the troughs or gaps visible in the same Figures indicate stronger non-dipolar contributions compared to the Pacific. This observation is consistent with previous studies reporting a persistent lower contribution to the dipole in the Atlantic hemisphere (de Oliveira et al., 2024). Our analysis based on the spatial distribution of null intensity gradient contours provides a specific perspective on non-dipolar contributions to the location of geomagnetic surface intensity minima. It is also in agreement with persistent strong non-dipolar CMB field in the South Atlantic (Constable et al., 2016).

The distribution of $\frac{\partial F}{\partial \phi} = 0$ contours shown in Figure 10a is reminiscent of the wavenumber 2 dominance in the radial magnetic field. These features can be explained by heterogeneous heat flux at the CMB (Amit et al., 2015), where lateral variations in lower mantle temperature are dominated by a degree and order 2 spherical harmonic (Masters et al., 2000). At the CMB, two intense geomagnetic flux patches at high latitudes of each hemisphere are thought to be the outcome of this $Y_2^2$ ingredient in the CMB heat flux (e.g., Gubbins, 2003). Our results show a signature of this mantle control on the geodynamo at Earth's surface.

Overall, it should be noted that the HistKalmag model relies on archeomagnetic data, which are sparsely distributed (Arneitz et al., 2017). In particular, the archeomagnetic data density is relatively low in the Pacific Hemisphere and in oceanic regions. After 1500 CE, the addition of ships log data improves the spatial coverage. Therefore, caution should be exercised when interpreting results derived from these earlier periods.

Our topological algorithm, which we applied to geomagnetic surface intensity minima, may potentially be applied to other research domains. It may be used to better identify and track magnetic flux patches in core field models (Amit et al., 2011; Dumberry & Finlay, 2007; Terra-Nova et al., 2015) and numerical dynamo simulations (Amit et al., 2010) as well as magnetic pole locations at Earth's surface (Livermore et al., 2020). It can also be applied to characterize the kinematics of mantle plumes (Labrosse, 2002; Schubert et al., 2004). Possible applications of our algorithm to track changes in size of atmospheric tropical cyclones (e.g., Simpson, 1974; Irish et al., 2008) or large-scale ocean eddies (e.g., Jeong and Hussain, 1995; Isern-Fontanet et al., 2003) may also be envisioned.

## Conflict of Interest

The authors declare no conflicts of interest relevant to this study.

## Availability Statement

All codes used for figure generation and for calculating the characteristics of surface intensity minima are publicly available at https://doi.org/10.5281/zenodo.18460414 (Yue et al., 2026).

**Acknowledgments**

This work was supported by the National Natural Science Foundation of China (No. 42388101). H.A. and F.T.-N. acknowledge the financial support from the French Agence Nationale de Recherche, project DYRE-COMB (Grant ANR-22-CE49-0016-01). V.M. thanks the Grants 2023/02667-4 and 2025/00343-2, São Paulo Research Foundation (FAPESP). We thank two anonymous reviewers for their constructive comments that improved the manuscript.

## References

Amit, H., Aubert, J., & Hulot, G. (2010). Stationary, oscillating or drifting mantle-driven geomagnetic flux patches? *Journal of Geophysical Research*, *115*(B7), B07108. https://doi.org/10.1029/2009jb006542

Amit, H., Choblet, G., Olson, P., Monteux, J., Deschamps, F., Langlais, B., & Tobie, G. (2015). Towards more realistic core-mantle boundary heat flux patterns: a source of diversity in planetary dynamos. *Progress in Earth and Planetary Sciences*, *2*(26). https://doi.org/10.1186/s40645-015-0056-3

Amit, H., Korte, M., Aubert, J., Constable, C., & Hulot, G. (2011). The time-dependence of intense archeomagnetic flux patches. *Journal of Geophysical Research*, *116*(B12), B12106. https://doi.org/10.1029/2011jb008538

Amit, H., Terra-Nova, F., Lézin, M., & Trindade, R. (2021). Non-monotonic growth and motion of the South Atlantic anomaly. *Earth Planets and Space*, *73*(1), 38. https://doi.org/10.1186/s40623-021-01356-w

Arneitz, P., Leonhardt, R., Schnepp, E., Heilig, B., Mayrhofer, F., Kovacs, P., et al. (2017). The histmag database: Combining historical, archaeomagnetic and volcanic data. *Geophysical Journal International*, *210*(3), 1347–1359. https://doi.org/10.1093/gji/ggx245

Arsenović, P., Rozanov, E., Usoskin, I., Turney, C., Sukhodolov, T., McCracken, K., et al. (2024). Global impacts of an extreme solar particle event under different geomagnetic field strengths. *Proceedings of the National Academy of Sciences*, *121*(28), e2321770121. https://doi.org/10.1073/pnas.2321770121

Aubert, J. (2015). Geomagnetic forecasts driven by thermal wind dynamics in the Earth's core. *Geophysical Supplements to the Monthly Notices of the Royal Astronomical Society*, *203*(3), 1738–1751. https://doi.org/10.1093/gji/ggv394

Bloxham, J., Gubbins, D., & Jackson, A. (1989). Geomagnetic secular variation. *Philosophical Transactions of the Royal Society of London. Series A, Mathematical and Physical Sciences*, *329*(1606), 415–502.

Campuzano, S. A., Gómez-Paccard, M., Pavón-Carrasco, F. J., & Osete, M. L. (2019). Emergence and evolution of the South Atlantic anomaly revealed by the new paleomagnetic reconstruction SHAWQ2k. *Earth and Planetary Science Letters*, *512*, 17–26. https://doi.org/10.1016/j.epsl.2019.01.050

Constable, C., Korte, M., & Panovska, S. (2016). Persistent high paleosecular variation activity in southern hemisphere for at least 10 000 years. *Earth and Planetary Science Letters*, *453*, 78–86. https://doi.org/10.1016/j.epsl.2016.08.015

Constable, C., & Parker, R. (1988). Statistics of the geomagnetic secular variation for the past 5 my. *Journal of Geophysical Research*, *93*(B10), 11569–11581. https://doi.org/10.1029/jb093ib10p11569
de Oliveira, W. P., Hartmann, G. A., Terra-Nova, F., Pasqualon, N. G., Savian, J. F., Lima, E. F., et al. (2024). Long-term persistency of a strong non-dipole field in the south Atlantic. *Nature Communications*, *15*(1), 9447. https://doi.org/10.1038/s41467-024-53688-2
De Santis, A., & Qamili, E. (2015). Geosystemics: A systemic view of the Earth's magnetic field and the possibilities for an imminent geomagnetic transition. *Pure and Applied Geophysics*, *172*(1), 75–89. https://doi.org/10.1007/s00024-014-0912-x
De Santis, A., Qamili, E., & Wu, L. (2013). Toward a possible next geomagnetic transition? *Natural Hazards and Earth System Sciences*, *13*(12), 3395–3403. https://doi.org/10.5194/nhess-13-3395-2013
Dumberry, M., & Finlay, C. C. (2007). Eastward and westward drift of the Earth's magnetic field for the last three millennia. *Earth and Planetary Science Letters*, *254*(1–2), 146–157. https://doi.org/10.1016/j.epsl.2006.11.026
Erdmann, W., Kmita, H., Kosicki, J. Z., & Kaczmarek, Ł. (2021). How the geomagnetic field influences life on Earth–An integrated approach to geomagnetobiology. *Origins of Life and Evolution of the Biosphere*, *51*(3), 231–257. https://doi.org/10.1007/s11084-021-09612-5
Finlay, C. C., Kloss, C., & Gillet, N. (2025). Core field changes from eleven years of swarm satellite observations. *Physics of the Earth and Planetary Interiors*, *368*, 107447. https://doi.org/10.1016/j.pepi.2025.107447
Finlay, C. C., Kloss, C., Olsen, N., Hammer, M. D., Tøffner-Clausen, L., Grayver, A., & Kuvshinov, A. (2020). The CHAOS-7 geomagnetic field model and observed changes in the south Atlantic anomaly. *Earth Planets and Space*, *72*(1), 156. https://doi.org/10.1186/s40623-020-01252-9
Finlay, C. C., Maus, S., Beggan, C., Bondar, T. N., Chambodut, A., Chernova, T., et al. (2010). International geomagnetic reference field: The eleventh generation. *Geophysical Journal International*, *183*(3), 1216–1230. https://doi.org/10.1111/j.1365-246x.2010.04804.x
Gallet, Y., Hulot, G., Chulliat, A., & Genevey, A. (2009). Geomagnetic field hemispheric asymmetry and archeomagnetic jerks. *Earth and Planetary Science Letters*, *284*(1–2), 179–186. https://doi.org/10.1016/j.epsl.2009.04.028
Gao, J., Korte, M., Panovska, S., Rong, Z., & Wei, Y. (2022). Geomagnetic field shielding over the last one hundred thousand years. *Journal of Space Weather and Space Climate*, *12*, 31. https://doi.org/10.1051/swsc/2022027
Gauss, C. F. (1833). Intensitas vis magneticae terrestris ad mensuram absolutam revocata. In *Werke: Fünfter band* (pp. 79–118). Springer.
Gubbins, D. (2003). Thermal core-mantle interactions: Theory and observations. In V. Dehant, K. Creager, S. Karato, & S. Zatman (Eds.), *Earth's core: Dynamics, structure and rotation*. AGU Geodynamics Series - American Geophysical Union.
Hartmann, G. A., & Pacca, I. G. (2009). Time evolution of the South Atlantic magnetic anomaly. *Anais da Academia Brasileira de Ciências*, *81*(2), 243–255. https://doi.org/10.1590/s0001-37652009000200010
He, F., Wei, Y., Maffei, S., Livermore, P. W., Davies, C. J., Mound, J., et al. (2021). Equatorial auroral records reveal dynamics of the paleo-West Pacific geomagnetic anomaly. *Proceedings of the National Academy of Sciences*, *118*(20), e2026080118. https://doi.org/10.1073/pnas.2026080118
He, F., Wei, Y., & Wan, W. (2020). Equatorial Aurora: The aurora-like airglow in the negative magnetic anomaly. *National Science Review*, *7*(10), 1606–1615. https://doi.org/10.1093/nsr/nwaa083
Heirtzler, J. (2002). The future of the south Atlantic anomaly and implications for radiation damage in space. *Journal of Atmospheric and Solar-Terrestrial Physics*, *64*(16), 1701–1708. https://doi.org/10.1016/s1364-6826(02)00120-7
Hellio, G., & Gillet, N. (2018). Time-correlation-based regression of the geomagnetic field from archeological and sediment records. *Geophysical Journal International*, *214*(3), 1585–1607. https://doi.org/10.1093/gji/ggy214
Huder, L., Gillet, N., Finlay, C. C., Hammer, M. D., & Tchoungui, H. (2020). COV-OBS. x2: 180 years of geomagnetic field evolution from ground-based and satellite observations. *Earth Planets and Space*, *72*(1), 160. https://doi.org/10.1186/s40623-020-01194-2
Hulot, G., Eymin, C., Langlais, B., Mandea, M., & Olsen, N. (2002). Small-scale structure of the geodynamo inferred from oersted and Magsat satellite data. *Nature*, *416*(6881), 620–623. https://doi.org/10.1038/416620a
Hunter, J. D. (2007). Matplotlib: A 2D graphics environment. *Computing in Science & Engineering*, *9*(3), 90–95. https://doi.org/10.1109/MCSE.2007.55
Irish, J. L., Resio, D. T., & Ratcliff, J. J. (2008). The influence of storm size on hurricane surge. *Journal of Physical Oceanography*, *38*(9), 2003–2013. https://doi.org/10.1175/2008jpo3727.1
Isern-Fontanet, J., García-Ladona, E., & Font, J. (2003). Identification of marine eddies from altimetric maps. *Journal of Atmospheric and Oceanic Technology*, *20*(5), 772–778. https://doi.org/10.1175/1520-0426(2003)20<772:iomefa>2.0.co;2
Jeong, J., & Hussain, F. (1995). On the identification of a vortex. *Journal of Fluid Mechanics*, *285*, 69–94.
Labrosse, S. (2002). Hotspots, mantle plumes and core heat loss. *Earth and Planetary Science Letters*, *199*(1–2), 147–156. https://doi.org/10.1016/s0012-821x(02)00537-x
Lézin, M., Amit, H., Terra-Nova, F., & Wardinski, I. (2023). Mantle-driven north–south dichotomy in geomagnetic polar minima. *Physics of the Earth and Planetary Interiors*, *337*, 107000. https://doi.org/10.1016/j.pepi.2023.107000
Livermore, P. W., Finlay, C. C., & Bayliff, M. (2020). Recent north magnetic pole acceleration towards Siberia caused by flux lobe elongation. *Nature Geoscience*, *13*(5), 387–391. https://doi.org/10.1038/s41561-020-0570-9
Masters, G., Laske, G., Bolton, H., & Dziewonski, A. (2000). The relative behavior of shear velocity, bulk sound speed, and compressional velocity in the mantle: Implications for chemical and thermal structure. *Geophysical Monograph Series*, *117*, 63–87.
Meier, M. M., Berger, T., Jahn, T., Matthiä, D., Plettenberg, M. C., Scheibinger, M., et al. (2023). Impact of the South Atlantic Anomaly on radiation exposure at flight altitudes during solar minimum. *Scientific Reports*, *13*(1), 9348. https://doi.org/10.1038/s41598-023-36190-5
Nilsson, A., Nguyen, L., Panovska, S., Herbst, K., Zheng, M., Suttie, N., & Muscheler, R. (2024). Holocene solar activity inferred from global and hemispherical cosmic-ray proxy records. *Nature Geoscience*, *17*(7), 654–659. https://doi.org/10.1038/s41561-024-01467-5
Nilsson, A., Suttie, N., Korte, M., Holme, R., & Hill, M. (2020). Persistent westward drift of the geomagnetic field at the core–mantle boundary linked to recurrent high-latitude weak/reverse flux patches. *Geophysical Journal International*, *222*(2), 1423–1432. https://doi.org/10.1093/gji/ggaa249
Nilsson, A., Suttie, N., Stoner, J. S., & Muscheler, R. (2022). Recurrent ancient geomagnetic field anomalies shed light on future evolution of the South Atlantic Anomaly. *Proceedings of the National Academy of Sciences*, *119*(24), e2200749119. https://doi.org/10.1073/pnas.2200749119
Olson, P., & Amit, H. (2006). Changes in earth's dipole. *Naturwissenschaften*, *93*(11), 519–542. https://doi.org/10.1007/s00114-006-0138-6
Pan, Y., & Li, J. (2023). On the biospheric effects of geomagnetic reversals. *National Science Review*, *10*(6), nwad070. https://doi.org/10.1093/nsr/nwad070
Pavón-Carrasco, F. J., & De Santis, A. (2016). The South Atlantic Anomaly: The key for a possible geomagnetic reversal. *Frontiers in Earth Science*, *4*, 188187. https://doi.org/10.3389/feart.2016.00040
Rao, U. (1980). Crucial role of the magnetic field in the evolution of life. *Pramana*, *15*(1), 33–43. https://doi.org/10.1007/bf02847908
Rother, M., Korte, M., Morschhauser, A., Vervelidou, F., Matzka, J., & Stolle, C. (2021). The mag.num core field model as a parent for IGRF-13, and the recent evolution of the south Atlantic anomaly. *Earth Planets and Space*, *73*(1), 50. https://doi.org/10.1186/s40623-020-01277-0

Sanchez, S., Wicht, J., & Bärenzung, J. (2020). Predictions of the geomagnetic secular variation based on the ensemble sequential assimilation of geomagnetic field models by dynamo simulations. *Earth Planets and Space*, *72*(1), 157. https://doi.org/10.1186/s40623-020-01279-y

Schanner, M., Bohsung, L., Fischer, C., Korte, M., & Holschneider, M. (2023). The global geomagnetic field over the historical era: What can we learn from ship-log declinations? *Earth Planets and Space*, *75*(1), 96. https://doi.org/10.1186/s40623-023-01852-1

Schubert, G., Masters, G., Olson, P., & Tackley, P. (2004). Superplumes or plume clusters? *Physics of the Earth and Planetary Interiors*, *146*(1–2), 147–162. https://doi.org/10.1016/j.pepi.2003.09.025

Simpson, R. H. (1974). The hurricane disaster—Potential scale. *Weatherwise*, *27*(4), 169–186.

Tarduno, J. A., Watkeys, M. K., Huffman, T. N., Cottrell, R. D., Blackman, E. G., Wendt, A., et al. (2015). Antiquity of the south Atlantic anomaly and evidence for top-down control on the geodynamo. *Nature Communications*, *6*(1), 7865. https://doi.org/10.1038/ncomms8865

Tema, E., Santos, Y., Trindade, R., Hartmann, G., Hatakeyama, T., Terra-Nova, F., et al. (2023). Archaeointensity record of weak field recurrence in Japan: New data from late Yayoi and Kofun ceramic artefacts. *Geophysical Journal International*, *233*(2), 950–963.

Terra-Nova, F., & Amit, H. (2020). Magnetic boundary layers in numerical dynamos with heterogeneous outer boundary heat flux. *Physics of the Earth and Planetary Interiors*, *309*, 106589. https://doi.org/10.1016/j.pepi.2020.106589

Terra-Nova, F., & Amit, H. (2025). Necessary core-mantle boundary heat flux patterns for recovering the latitude of the south Atlantic Anomaly. *Journal of Geophysical Research: Solid Earth*, *130*(11), e2025JB031193. https://doi.org/10.1029/2025jb031193

Terra-Nova, F., Amit, H., & Choblet, G. (2019). Preferred locations of weak surface field in numerical dynamos with heterogeneous core-mantle boundary heat flux: Consequences for the South Atlantic Anomaly. *Geophysical Journal International*, *217*(2), 1179–1199. https://doi.org/10.1093/gji/ggy519

Terra-Nova, F., Amit, H., Hartmann, G. A., & Trindade, R. I. (2015). The time dependence of reversed archeomagnetic flux patches. *Journal of Geophysical Research: Solid Earth*, *120*(2), 691–704. https://doi.org/10.1002/2014jb011742

Terra-Nova, F., Amit, H., Hartmann, G. A., & Trindade, R. I. (2016). Using archaeomagnetic field models to constrain the physics of the core: Robustness and preferred locations of reversed flux patches. *Geophysical Journal International*, *206*(3), 1890–1913. https://doi.org/10.1093/gji/ggw248

Terra-Nova, F., Amit, H., Hartmann, G. A., Trindade, R. I., & Pinheiro, K. J. (2017). Relating the South Atlantic Anomaly and geomagnetic flux patches. *Physics of the Earth and Planetary Interiors*, *266*, 39–53. https://doi.org/10.1016/j.pepi.2017.03.002

Trindade, R. I., Jaqueto, P., Terra-Nova, F., Brandt, D., Hartmann, G. A., Feinberg, J. M., et al. (2018). Speleothem record of geomagnetic south Atlantic anomaly recurrence. *Proceedings of the National Academy of Sciences*, *115*(52), 13198–13203. https://doi.org/10.1073/pnas.1809197115

Wang, Y., Chen, S., Xu, K., Yan, L., Yue, X., He, F., & Wei, Y. (2021). Ancient auroral records compiled from Korean historical books. *Journal of Geophysical Research, Space Physics*, *126*(1), e2020JA028763. https://doi.org/10.1029/2020ja028763

Wei, Y., Pu, Z., Zong, Q., Wan, W., Ren, Z., Fraenz, M., et al. (2014). Oxygen escape from the Earth during geomagnetic reversals: Implications to mass extinction. *Earth and Planetary Science Letters*, *394*, 94–98. https://doi.org/10.1016/j.epsl.2014.03.018

Yue, Y., Gao, J., He, F., Wei, Y., Cai, S., Wang, H., et al. (2024). Evolution and disappearance of the paleo-West Pacific anomaly: Implications to the future of South Atlantic Anomaly. *Physics of the Earth and Planetary Interiors*, *353*, 107214. https://doi.org/10.1016/j.pepi.2024.107214

Yue, Y., Terra-Nova, F., Amit, H., Marum, V., Wang, Y., & Wei, Y. (2026). Time dependence of multiple geomagnetic surface intensity minima. *Zenodo*. https://doi.org/10.5281/zenodo.18460414